Astronomy & Astrophysics

XMM-Newton and INTEGRAL analysis of the Ophiuchus cluster of galaxies

J. Nevalainen[1], D. Eckert[2], J. Kaastra[3], M. Bonamente[4], and K. Kettula[1]

[1] Observatory, University of Helsinki, Finland
    e-mail: Jukka.H.Nevalainen@helsinki.fi
[2] ISDC Data Centre for Astrophysics, Geneva Observatory, University of Geneva, Switzerland
[3] SRON Netherlands Institute for Space Research, The Netherlands
[4] University of Alabama in Huntsville, Huntsville, USA; NASA National Space and Technology Center, Huntsville, USA

ABSTRACT

Aims. We investigated the non-thermal hard X-ray emission in the Ophiuchus cluster of galaxies. Our aim is to characterise the physical properties of the non-thermal component and its interaction with the cosmic microwave background.
Methods. We performed spatially resolved spectroscopy and imaging using XMM-Newton data to model the thermal emission. Combining this with INTEGRAL ISGRI data, we modelled the 0.6−140 keV band total emission in the central 7 arcmin region.
Results. The models that best describe both PN and ISGRI data contain a power-law component with a photon index in a range 2.2−2.5. This component produces ∼10% of the total flux in the 1−10 keV band. The pressure of the non-thermal electrons is ∼1% of that of the thermal electrons. Our results support the scenario whereby a relativistic electron population, which produces the recently detected radio mini-halo in Ophiuchus, also produces the hard X-rays via inverse compton scattering of the CMB photons. The best-fit models imply a differential momentum spectrum of the relativistic electrons with a slope of 3.4−4.0 and a magnetic field strength $B = 0.05−0.15$ μG. The lack of evidence for a recent major merger in the Ophiuchus centre allows the possibility that the relativistic electrons are produced by turbulence or hadronic collisions.

Key words. galaxies: clusters: individual: Ophiuchus – X-rays: galaxies: clusters – techniques: spectroscopic

1. Introduction

Non-thermal hard X-ray emission has been detected in several clusters of galaxies over the past few years (see Rephaeli et al. 2008, for a recent review). Since the detections have remained at the level of a few σ, many models still remain as valid explanations for the phenomenon. The most popular explanation is the inverse compton scattering of the cosmic microwave background photons with the relativistic electrons in the cluster (e.g. Sarazin et al. 1988). In this model, the CMB photon ends up in the hard X-ray band since its energy increases by a factor of ∼10⁸ via the scattering. In primary models, the relativistic electrons are originally thermal electrons that have been accelerated by a cluster merger (e.g. Sarazin & Lieu 1998) or turbulence (e.g. Brunetti et al. 2001, 2004). In secondary models, the acceleration comes from hadronic collisions (e.g. Dennison 1980; Pfrommer & Ensslin 2004).

Recently a radio mini-halo was detected in the centre of the Ophiuchus cluster with the VLA at 1.4 GHz (Govoni et al. 2009; Murgia et al. 2009). This proved the existence of a population of relativistic electrons in Ophiuchus. Ophiuchus is a hot ($T \sim 9$ keV) nearby ($z = 0.028$) cluster located close to the Galactic centre ($l \sim 1°$, $b \sim 9°$). Consistently, INTEGRAL detected excess emission over the thermal component at a 4−6σ level in the 20−80 keV energy band in the Ophiuchus cluster (Eckert et al. 2008). The analysis was lacking a sensitive instrument for modelling the thermal component at lower energies, but the excess was nevertheless consistent with having a non-thermal origin.

Our aim in this work is to improve the modelling of the emission in the Ophiuchus centre utilising spatially resolved XMM-Newton spectroscopy. In this work we use the EPIC instruments PN for spectral analysis and MOS2 for imaging of the central 7 arcmin region of the Ophiuchus cluster. Because of the limitations of the spatial capability of INTEGRAL, we cannot exclude regions of complex temperature structure. Rather, we examine the spatially resolved XMM-Newton data in order to obtain an accurate model for the thermal emission to be used later with the INTEGRAL data. We also update the INTEGRAL analysis with additional data.

2. XMM-Newton data reduction

We observed the Ophiuchus cluster with XMM-Newton on September 2, 2007, during revolution 1416. The observation ID is 0505150101. The PN instrument was operated in extended full frame mode and the EPIC instruments used the medium optical filter.

2.1. Processing the data

We processed the raw data with the SAS version xmmsas_20080701_1801-8.0.0 tools epchain and emchain with the default parameters in order to produce the event files. We used the latest calibration information in October 2008. We also generated the simulated out-of-time event file, which we later used to subtract the events registered during readout of a CCD from PN spectra. We filtered the event files excluding
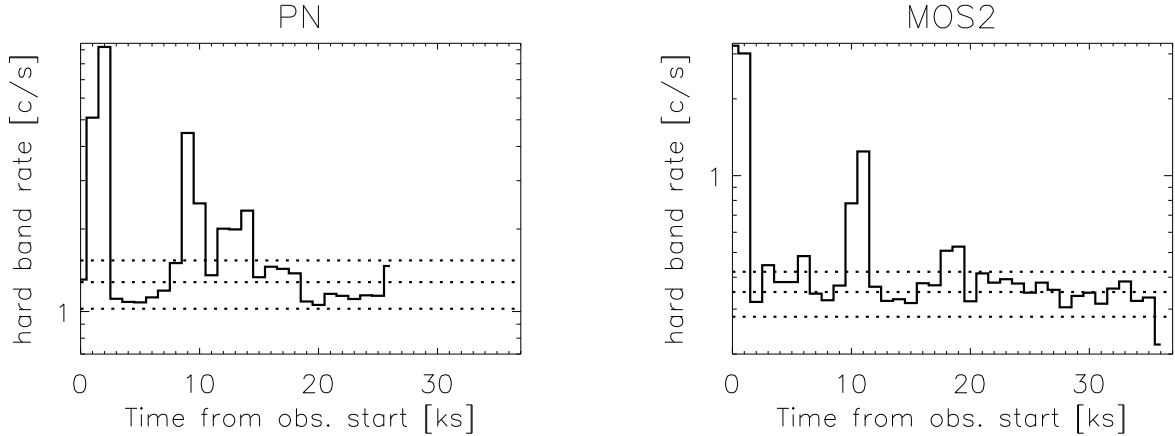
PN   MOS2

Fig. 1. The histogram shows the light curve of Ophiuchus in the full FOV in 1000 ks time bins in the hard band ($E > 10$ keV for PN, *left panel* and $E > 9.5$ keV for MOS2, *right panel*). The dotted horizontal lines show the adopted quiescent level.

bad pixels and CCD gaps. We further filtered the event files including only patterns 0–4 (PN) and 0–12 (MOS). We used the evselect-3.58.7 tool to extract spectra, images, and light curves, while excluding the regions contaminated by bright point sources. We used the rmfgen-1.55.1 and arfgen-1.75.5 tools to produce energy redistribution files and the auxiliary response files.

2.2. Background

We extracted the hard band ($E > 10$ keV for PN, $E > 9.5$ keV for MOS2) light curves of the full field-of-view region in order to examine the behaviour of the particle background (see Fig. 1). We found that while the fraction of the exposure time containing the flares was small, the quiescent level exceeded that of the closed filter sample (Nevalainen et al. 2005) by a factor of ~2. Thus, instead of using the quiescent level from blank sky compilations we defined it as a level exceeding the light curve minimum by 20%. We accepted such periods, during which the hard band count rate was within ±20% of the quiescent level. This results in 16 ks and 28 ks of useful exposure time for PN and MOS2, respectively.

Since Ophiuchus is very bright and its spectrum is relatively hard, there is some cluster signal even at a photon energy of 10 keV (see Fig. 2). At higher energies ($E > 14$ keV for PN; $E > 10.5$ keV for MOS2), the spectrum of Ophiuchus is consistent with that of the scaled closed filter sample, by a factor of 1.77 and 1.93 for PN and MOS2, respectively. Thus, in the following we use the closed filter spectrum, multiplied by the above factor to remove the particle background from the data.

Since Ophiuchus fills the whole FOV we cannot obtain a local estimate for the sky background. Neither are the blank sky compilations useful, since the Galactic emission and absorption are very high due to Ophiuchus being located close to the Galactic Centre. We thus used the HEASARC tool based on ROSAT All Sky Survey data to obtain the spectrum of the Galaxy. We used fields with centre within 0.5–1.0 degree around the Ophiuchus centre. We modelled the spectrum using an unabsorbed MEKAL for the Local Hot Bubble, and an absorbed MEKAL + power-law to account for the emission of the Galactic halo and the cosmic X-ray background. We kept the photon index fixed to 1.41 as found in the measurements by De Luca et al. (2004). The best-fit MEKAL temperatures were in the range 0.1–0.2 keV. The obtained value and 1σ statistical
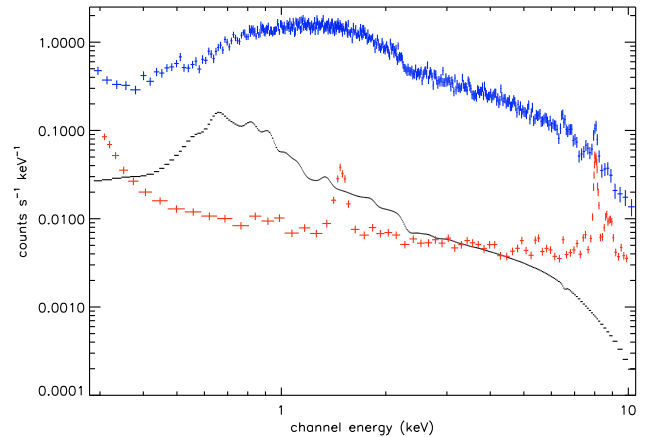

Fig. 2. The total PN emission spectrum obtained within the 6.5–7.0 arcmin annulus, containing the cluster and background components, is shown with blue crosses. Also shown separately are the background components, i.e. the detector background (red crosses) and the sky background (black curve).

uncertainty interval for *NH* is 0.46 [0.39–0.66] $\times 10^{21}$ cm^{-2}, much higher than that derived with the radio measurements of HI at 21 cm (Kalberla et al. 2005). We will address this issue in detail in Sect. 5.

Compared to the background, the cluster emission is strong even at the outermost annulus (with radii 6.5–7.0 arcmin) used in this work, where the cluster is the faintest (see Fig. 2). In order to keep the detector and sky background emission below 10% of the cluster signal, we limited our spectral analysis to photons with energy in the range 0.6–7.4 keV in the following.

3. INTEGRAL data reduction

An analysis of INTEGRAL data on the cluster was already presented in Eckert et al. (2008). We aim here at complementing the results presented in this paper by the addition of new data and a very careful study of the systematic effects which might affect the results.

3.1. Data selection and spectral extraction

The IBIS/ISGRI instrument (Lebrun et al. 2003) on board *INTEGRAL* (Winkler et al. 2003) is a wide-field (29° × 29°)

coded-mask instrument operating in the 15−400 keV band. It is made of an array of 128×128 CdTe pixels and it features an angular resolution of 12 arcmin *FWHM*. Thanks to the observing strategy of *INTEGRAL*, which spends a significant fraction of its observing time in the Galactic Bulge region, and to the large field-of-view (FOV), the available *INTEGRAL* exposure time on the Ophiuchus cluster ($l = 0.5°$, $b = 9.0°$) is large. For this analysis, we used all publicly-available data from the *INTEGRAL* archive, restricting to the observations where the source was at most 8° offset from the pointing position, and we filtered out the data where the background rate was found to be more than 3 times larger than the average (e.g. because of solar flares). Overall, our data set comprises ~1900 individual pointings, for a total of 3 Ms of high-quality data on the source. This allows us to detect the source with high significance (53σ) in the 15−140 keV band (see Fig. 3).

To analyse the data, we used the standard Offline Scientific Analysis (OSA) package, version 7.0, distributed by ISDC (Courvoisier et al. 2003). The analysis of the ISGRI data in this region is made difficult by the presence of many point sources in the field (e.g. the bright Low-Mass X-ray Binary Scorpius X-1), whose shadow pattern overlaps with that of the Ophiuchus cluster. In order to take the contribution of other sources in the FOV into account, we prepared a catalogue comprising the 37 brightest sources detected in the mosaic images of the region, and used this catalogue as input to the spectral extraction tool, which then performs a multi-parameter fit of the shadow pattern of each sources to the raw detector images. In addition, it is known that the presence of screws and glue strips attaching the IBIS mask to the supporting structure can introduce systematic effects in the presence of very bright sources. To get rid of this systematic effect, we identified the mask areas where screws and glue are absorbing incoming photons, and we ignored the pixels which were illuminated by these areas for the three brightest sources in the field (Scorpius X-1, 4U 1700-377 and GRS 1758-258). As a cross check, we also extracted the ISGRI spectra directly by fitting the mosaic images, although this method is known to be less reliable for flux estimates. Except for the first bin (15−18 keV), where the ISGRI calibration is known to be uncertain due to the pixel low threshold, there is excellent agreement between the spectra extracted with the 2 methods.

In order to estimate the contamination of the spectra by the bright objects in the FOV, we extracted ISGRI spectra at 10 random positions within a radius of 2 degrees from the Ophiuchus cluster. As expected, no detection was obtained for any of the 10 observations and the data were distributed normally in all energy bins (see Fig. 3). According to the latest *INTEGRAL* cross-calibration report based on OSA 7.0 (Jourdain et al. 2008), the systematic uncertainties on the ISGRI RMF and ARF calibration are at 1% level. As a conservative estimate for the systematic uncertainties on the energy calibration of ISGRI, a flat 2% systematic error has been added to the spectra presented in Fig. 3. In any case, we note that the level of statistical uncertainties is always significantly higher than 2%, so the uncertainties on the energy calibration do not affect significantly the results.

For the detailed analysis of the spectra presented hereafter, we restrict to the spectrum extracted using the standard spectral extraction method, and we ignore the first energy bin (15−18 keV) because of uncertain calibration.

4. XMM-Newton imaging analysis

We used MOS2 for the imaging, since that EPIC instrument has the smallest fraction (4%) of the central 7 arcmin region
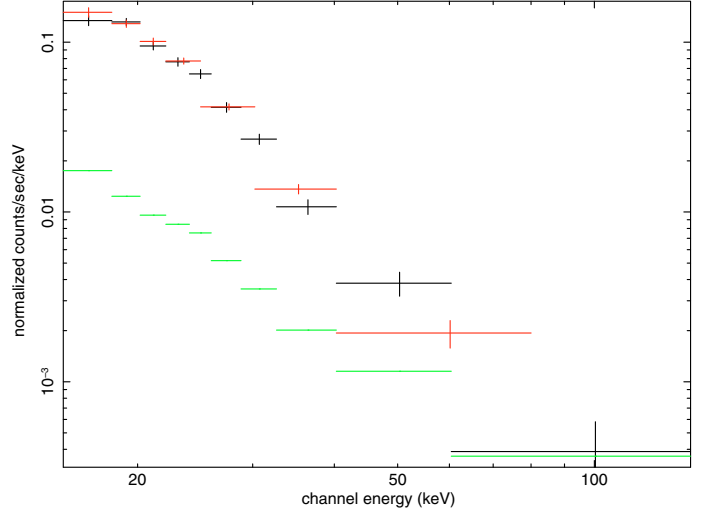

Fig. 3. *INTEGRAL*/ISGRI spectrum of the Ophiuchus cluster extracted with 2 different methods (black: standard OSA spectral extraction tool, red: extraction from mosaic images). The green lines show the 2-σ noise level estimated from 10 random positions within a radius of 2 degrees around the source.

obscured by the dead area due to e.g. CCD gaps and bad pixels. We accumulated an image in the 0.5−7.0 keV band in 5 arcsec bins. We subtracted the particle background component from the imaging data using the closed cover compilation of Nevalainen et al. (2005). We then produced the exposure map using the SAS *eexpmap-4.4.1* tool and by dividing the imaging data with the exposure map, we produced a vignetting corrected surface brightness map. We further used the exposure map to produce a mask file for filtering out the data close to the CCD gaps.

4.1. Brightness distribution

The resulting image (Fig. 4) shows that the brightness distribution in the central region is elliptical, with an axis ratio of ~0.7. The location of the brightness peak is offset from the centroid of the elliptical brightness distribution by ~1.5 arcmin, i.e. 50 kpc in the plane of the sky. The X-ray morphology and the centroid shift do vary with time in the cluster merger simulations (e.g. Poole et al. 2006) and thus this shift may be taken as an indication of merger activity in the Ophiuchus centre. However, the variation due to merger details prohibits us to use the above values to estimate the time passed since the possible major merger in the centre of Ophiuchus.

There are some deviations from the azimuthally symmetric brightness distribution. At 3.5−7 arcmin distance from the X-ray peak towards the south-east the surface brightness is lower than in the rest of the cluster at same radii. The edge-like feature of the brightness distribution at ~1.2 arcmin (=40 kpc) distance from the X-ray peak towards south and west coincides with the density discontinuity found in Chandra data (Markevitch et al. 2007), who interpreted the structure as a cold front. A detailed analysis of density discontinuities at small angular scales is not warranted with XMM-Newton due to its relatively large PSF. The XMM-Newton data indicate that a surface brightness jump bigger than 10% in the central 2 arcmin region towards south is excluded.

We extracted a surface brightness profile in co-centric annuli of 12 arcsec width centred at the X-ray peak location (see Fig. 5). The profile is not well fitted with a single-β model
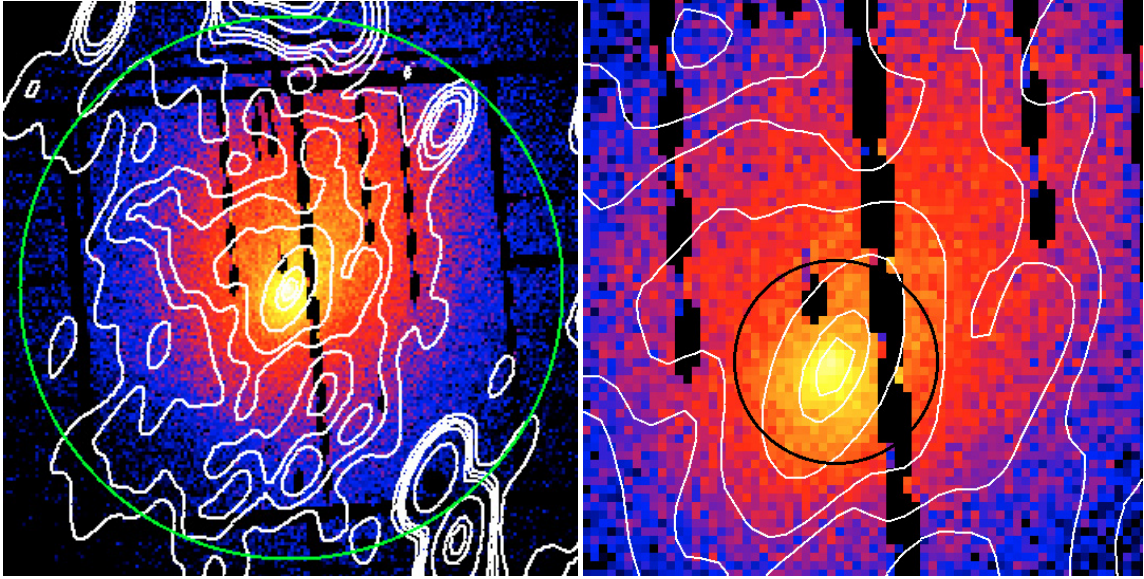
Fig. 4. Vignetting-corrected MOS2 image of the Ophiuchus cluster centre in the 0.5−7.0 keV band. The pixel size is 5″. The white curves show radio contours at 1.4 GHz (from Govoni et al. 2009). In the *left panel* the green circle shows the extraction region ($r = 7$ arcmin) for the XMM-Newton spectrum. The *right panel* shows a close-up of the central region. The circle denotes the central $r = 1$ arcmin (=33 kpc) region.
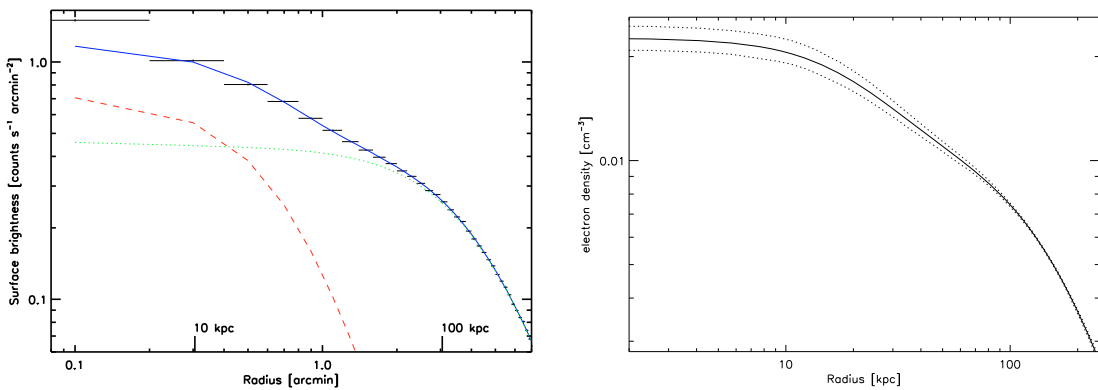

Fig. 5. In *the left panel* the black crosses show the surface brightness data of MOS2 centred at the X-ray peak. The best-fit narrow and wide β components are shown with a dashed red line and a dotted green line, respectively. The blue line is the sum of the two β-components. The models are extrapolated to $r < 0.2$ arcmin (=7 kpc). The derived best-fit gas density profile in shown in *the right panel* as a thick line, together with the uncertainties due to the statistical errors of the parameters at 1σ level.

(Cavaliere & Fusco-Femiano 1976) and thus we used the double-β model, which describes the data well in the radial range 12″−7′ with core radii $r_{\rm core,1} = 0.7 \pm 0.1$ arcmin and $r_{\rm core,2} = 4.9 \pm 0.2$ arcmin in the two components (narrow and broad β-components), while the common β-parameter obtains a value of 0.74 ± 0.02.

4.2. Cool core

A natural explanation of the emission in the narrow β-component is the cooling of the intra-cluster gas. Suzaku analysis of Ophiuchus suggested that Ophiuchus has a cool core (Fujita et al. 2008). The typical cooling radius of 70 kpc (=2 arcmin) found in a cluster sample by the Chandra satellite (Vikhlinin et al. 2006) is also consistent with the extent of the central excess.

To examine in detail the central emission we accumulated a PN spectrum within a $r = 30″$ radius circle around the X-ray peak (for more details about the spectral fitting, see Sect. 5). The spectrum was not acceptably fitted with a single temperature model, and we thus experimented with a two-temperature

model. Since the metal abundance of the cool component was poorly constrained, we fixed it to 1.0 in Solar units. This model yielded an acceptable solution whereby ∼90% of the total emission originates from (hot) gas with $T = 6.7 \pm 0.4$ keV, while the rest is due to a (cool) component with $T = 1.7 \pm 0.1$ keV.

The temperature of the hot component is ∼30% lower than that outside the central 1 arcmin region (see below). Such a temperature drop is consistent with those found in the Chandra sample of clusters (Vikhlinin et al. 2006). The emission measure of the hot component yields a central proton density of ∼2×10^{-2} cm^{-3} (see Fig. 5 for the electron density profile) corresponding to a cooling time of 3×10^9 yr. This argues against a strong recent merger.

However the cooling radius in Ophiuchus is quite small (∼30 kpc) compared to other clusters. Also, the proton density decreases only by 40% between $r = 0$ and $r = 1.0$ arcmin which increases the cooling time by a factor of 1.7, i.e. to 5×10^9 yr at $r = 1$ arcmin. The rapid drop in the density (and the rapid increase in cooling time) begins at $r = 3$ arcmin where one would assume the cooling to end. Note that the radius 3 arcmin (=100 kpc) is better consistent with the cooling

radii in the Chandra sample. Thus it appears that the 1−3 arcmin temperatures are too high for the typical cool core cluster.

4.3. CD galaxy

As noted in Perez-Torres et al. (2009), the X-ray peak location is consistent with that of an elliptical cD galaxy 2MASX J17122774-2322108 (Hasegawa et al. 2000). The extent of the central excess on top of the broad β-component (~2 arcmin) corresponds to 70 kpc at the distance of Ophiuchus. This is consistent with the maximal extent of X-ray haloes of cD galaxies (e.g. Matsushita 2001). Also, in the innermost 12″ the surface brightness data exceeds the model by 30%, indicative of a central point source which may be the nucleus of the cD galaxy. Thus the spatial distribution of the X-ray brightness is consistent with a central cD galaxy.

The temperature and the 0.2−2.0 keV band luminosity (1.8×10^{42} erg s^{-1}) of the cool component in the above fit (Sect. 4.2) are consistent with those in several cD galaxies studied in e.g. Matsushita (2001). The surface brightness profile derived above shows that the flux in the narrow β-component in the central 30″ region exceeds that of the broad β-component. Since the cool component in the above fit constitutes only 10% of the central flux, it does not explain the central brightness excess as modelled with the narrow β-model. Rather, the flux of the cool component is consistent with the point-source-like excess flux in the central 12″ region on top of the double-β model prediction (see Fig. 5). We thus attribute the cD galaxy emission with the low temperature point source at the cluster centre.

5. XMM-Newton spectral analysis

In order to examine the spatial distribution of the temperature of the intra-cluster gas we performed spatially resolved spectroscopy using PN data. We divided the central $r = 7$ arcmin region into annuli of 0.5−1 arcmin width and further divided the annuli at $r = 1−7$ arcmin into four sectors. We centred the annuli on the surface brightness peak. We extracted spectra in these regions and fitted the 0.5−7.4 keV band data with a single-temperature MEKAL model, except in the central $r = 0.5$ arcmin region, where an additional thermal component is required (as discussed in Sect. 4.2). We fitted the spectra using XSPEC version 12.5.0s. We adopted the solar abundance table of Anders & Grevesse (1989). We note that we assume in this modelling that the non-thermal component does not affect significantly the derived spatial distribution of the thermal properties, i.e. that the non-thermal component contributes insignificantly in the PN band compared to the thermal component or that the spatial distribution of the non-thermal component is azimuthally symmetric.

5.1. NH

We attempted to model the spectra including a WABS absorption model which uses the photo-electric absorption cross sections of Morrison & McCammon (1983) and the relative element abundances of Anders & Ebihara (1982). However, we were unable to model the spectra acceptably when using the hydrogen column density $NH = 0.2 \times 10^{22}$ cm^{-2} as given by the 21 cm radio measurements of neutral hydrogen (HI) (Kalberla et al. 2005). Also, the best-fit temperatures are unrealistically high (see Table 1). Neither the absorption model PHABS nor the different tables for

the cross section or relative abundances in XSPEC improved the fits.

While the HI-based NH value (Kalberla et al. 2005) varies in the range 0.16−0.23 $\times 10^{22}$ cm^{-2} in the fields centred within 1° of the Ophiuchus centre, the PN data require a significantly larger amount of absorption ($NH = 0.3−0.4 \times 10^{22}$ cm^{-2}, see Table 1). Similar results were reported in the Suzaku analysis of Ophiuchus (Fujita et al. 2008). We also found that the modelling of the soft X-ray sky background using ROSAT All Sky Survey data close to Ophiuchus yielded a higher value $NH = 0.46 \times 10^{22}$ cm^{-2} (Sect. 2.2). Note that the NH values of Kalberla et al. (2005) are derived under the assumption that the HI 21-cm line is optically thin, which may be violated at latitudes within 10° of the Galactic equator and thus the values may be underestimated[1].

At low Galactic latitudes molecular material may yield significant absorption, and yet remain undetected in radio surveys since it does not contribute to the 21 cm line. This is quite probable for the Ophiuchus region, which is a well known site of star formation. The absorption in our energy band of 0.6−7.4 keV is dominated by heavier elements than hydrogen. We use the molecular hydrogen (H_2) as a tracer of molecular metals in the following. Unfortunately a direct measurement of the H_2 column density towards the Ophiuchus cluster is not reported in the literature. The measurements of the interstellar dust towards Ophiuchus can be used to estimate the total NH, since the dust is physically connected to the neutral and molecular hydrogen. Schlegel et al. (1998) mapped the density of dust in the Galaxy using IRAS 100 μm and DIRBE FIR data. Using the background galaxies they derived the dust extinction and yielded a reddening value of $E(B − V) = 0.585$ mag in the direction of Ophiuchus cluster.

The relation between $E(B − V)$ and total HI+H_2 density was calibrated using the L-α absorption measurements of stars with Copernicus-satellite (Bohlin et al. 1978). The relation with the above estimate for the reddening in Ophiuchus yields a total NH of 0.34×10^{22} cm^{-2}, much higher than the 21 cm value (0.2×10^{22} cm^{-2}), indicating that H_2 density is substantial, 35% of that of HI. The value of total NH is consistent with the highest X-ray absorption value in our work (see Fig. 6). Assuming that the metal to hydrogen abundance ratios in the molecular material are approximately Solar, the above consistence means that the molecular metal absorption is a viable explanation for the difference between the NH value obtained from X-ray absorption and radio 21 cm emission. In the following we thus account for the excess absorption by allowing NH to be a free parameter of the WABS model.

5.2. Temperature distribution

Fortunately we can also constrain the temperatures without the effect of NH uncertainties, utilising the monotonically decreasing Fe XXV/XXVI emission line ratio with temperature. In practise, we fitted the data with a MEKAL model in a narrow band (6.0−7.4 keV) containing both lines (redshifted to ~6.5 and ~6.8 keV at the distance of Ophiuchus), where the absorption is negligible. The drawback is that the number of photons in the above regions is too small in this narrow band for a statistically meaningful analysis. We thus used 1−3−5−7 arcmin annuli to examine the mean temperature with the Fe lines.

Most of the thus derived temperatures agree with those derived with the full band and free NH (see Fig. 6). This means that

---

[1] http://www.astro.uni-bonn.de/~webaiub/english/tools_labsurvey.php

Table 1. Single-temperature fits.

	NH fixed[a]		NH free[b]		
region[c]	T [keV]	χ^2/d.o.f	NH [10^{22} cm^{-2}]	T [keV]	χ^2/d.o.f
0′–0.5′[d]	79.9	987.0/284	0.35[0.34–0.35]	6.7[6.4–7.2]	209.0/283
0.5′–1′	23.0	1361.2/447	0.33[0.33–0.33]	7.7[7.5–7.9]	373.0/446
1′–2′ nw	33.5	740.9/332	0.32[0.31–0.32]	9.7[9.3–10.2]	242.5/331
1′–2′ sw	38.9	780.3/312	0.32[0.32–0.33]	10.0[9.5–10.5]	251.0/311
1′–2′ se	27.5	651.7/292	0.32[0.31–0.32]	9.1[8.7–9.5]	202.2/291
1′–2′ ne	36.7	762.7/301	0.33[0.32–0.33]	9.5[9.1–10.0]	248.0/300
2′–3′ nw	31.9	1128.6/417	0.33[0.33–0.34]	9.0[8.6–9.3]	301.1/416
2′–3′ sw	35.4	810.2/317	0.33[0.32–0.33]	9.6[9.2–10.1]	253.4/316
2′–3′ se	23.0	546.3/295	0.30[0.29–0.30]	9.4[9.0–9.9]	227.0/294
2′–3′ ne	30.7	703.7/298	0.32[0.31–0.32]	9.2[8.8–9.6]	250.6/297
3′–4′ nw	34.5	1255.8/465	0.33[0.33–0.34]	9.1[8.8–9.5]	362.3/464
3′–4′ sw	26.8	574.4/306	0.30[0.29–0.30]	10.2[9.7–10.7]	249.3/305
3′–4′ se	24.3	427.3/268	0.29[0.28–0.29]	10.1[9.6–10.8]	210.8/267
3′–4′ ne	24.2	704.2/312	0.31[0.31–0.32]	8.5[8.2–8.9]	257.9/311
4′–5′ nw	24.5	1104.2/457	0.32[0.31–0.32]	8.7[8.4–9.0]	374.5/456
4′–5′ sw	21.0	442.8/279	0.29[0.28–0.30]	9.4[9.0–9.9]	201.4/278
4′–5′ se	21.0	332.3/250	0.28[0.27–0.28]	10.3[9.7–11.0]	186.6/249
4′–5′ ne	25.6	571.2/284	0.31[0.30–0.31]	9.3[8.8–9.8]	207.3/283
5′–6′ nw	21.6	798.4/409	0.29[0.29–0.30]	9.4[9.0–9.8]	383.5/408
5′–6′ sw	24.4	448.7/264	0.29[0.29–0.30]	9.7[9.2–10.3]	199.3/263
5′–6′ se	21.5	296.8/215	0.28[0.27–0.28]	10.2[9.5–11.0]	178.6/214
5′–6′ ne	21.7	341.2/241	0.29[0.28–0.29]	9.5[9.0–10.2]	181.2/240
6′–7′ nw	22.9	492.7/309	0.28[0.28–0.29]	10.1[9.6–10.7]	243.7/308
6′–7′ sw	20.8	370.1/216	0.30[0.29–0.30]	8.9[8.4–9.5]	187.6/215
6′–7′ se	17.7	181.9/173	0.27[0.26–0.28]	9.3[8.7–10.1]	112.3/172
6′–7′ ne	24.9	241.6/203	0.28[0.27–0.29]	10.4[9.6–11.3]	122.4/202

[a] NH is fixed to the 21 cm measurement (=0.2×10^{22} cm^{-2}).
[b] NH is a free parameter.
[c] The values indicate the inner and outer radii while the letters indicate the direction of the spectrum extraction sector: North-West (nw), South-West (sw), South-East (se), and North-East (ne).
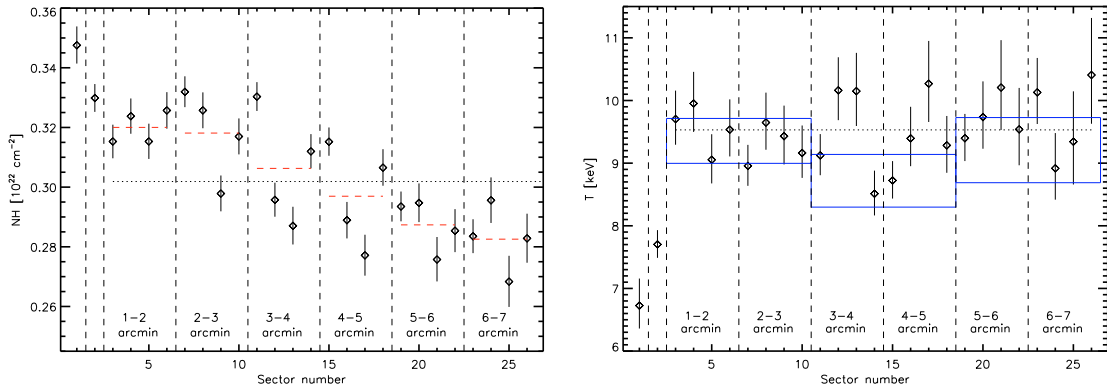[d] The model includes a component for the CD galaxy.

Fig. 6. The best-fit values and statistical uncertainties (diamonds and solid lines) for the free NH (*left panel*) and the temperature (*right panel*). The blue boxes show the temperatures derived using the Fe XXV/XXVI line ratio. The vertical dashed lines separate the different radial regions. For a given annulus, the sectors are numbered clock-wise from the North-West, except for "sectors" 1 and 2, which refer to the $r = 0.5$ arcmin circle and $r = 0.5-1.0$ arcmin annulus. The horizontal dashed and dotted lines show the azimuthal average values.

the NH enhancement towards the cluster centre is real and probably due to a chance superposition of the Ophiuchus center and a denser part of a Galactic molecular matter clump. The temperatures in sectors 12, 13 and 17 disagree with the azimuthal average, but only by $\sim 2\sigma$. Thus, we do not detect very significant azimuthal temperature variations in the central 7 arcmin region

of Ophiuchus. This implies that the central region of Ophiuchus is not disturbed by a recent major merger.

Utilising the azimuthal symmetry, we further examined the radial behaviour of the temperature in concentric annuli of 0.5 arcmin width and fitted the spectra with NH as a free parameter with a single-temperature MEKAL component (keeping
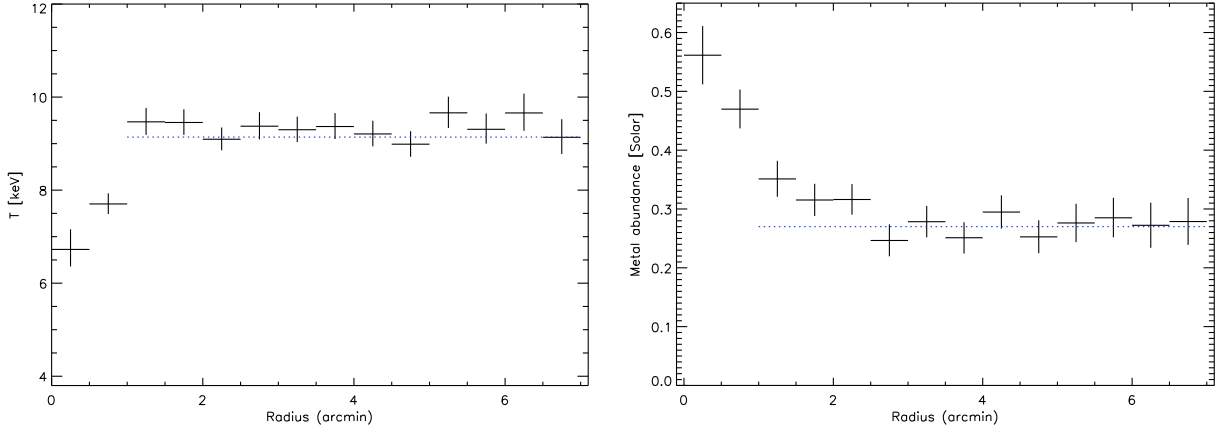
Fig. 7. The best-fit values and 1σ uncertainties of the temperature (*left panel*) and the metal abundance (*right panel*) profiles of Ophiuchus. The horizontal lines show the values obtained from a fit to a spectrum accumulated in a $1-7$ arcmin annulus.

the cool component in the centre as found above). At $1-7$ arcmin the profile is very flat, consistent with the value obtained from a fit to a single spectrum of the data in the radial range $1-7$ arcmin (9.1 ± 0.1 keV) (see Fig. 7). The central temperature drop (discussed above) is accompanied by the central increase of the metal abundance up to 0.6 Solar from the constant ~ 0.3 Solar at $r = 2-7$ arcmin, as observed in cool core clusters (e.g. Baldi et al. 2007).

5.3. Thermal model of the central 7 arcmin region

Using the best-fit double-β model for the flux distribution we estimated that 90% of the total flux in the central 7 arcmin region flux originates from the $1-7$ arcmin region. This is consistent with the emission measures obtained from the spectral fits to the spectra accumulated in the $0-1-7$ arcmin regions. Thus most of the emission is due to isothermal gas which simplifies the total emission modelling. Our final XMM-Newton based thermal model for the emission in the central 7 arcmin region of Ophiuchus consists of three thermal components. One of the components models the emission from the cD galaxy (as derived above), i.e. with temperature and metal abundances $T_1 = 1.7$ keV, $abund_1 = 1.0$ Solar. The second component describes the cool gas in the core, obtained with a fit to $0-1.0$ arcmin data while keeping the above cD component fixed. This component has parameters $T_2 = 7.3$ keV, $abund_2 = 0.50$ Solar. The third component is for the isothermal gas in the $1-7$ arcmin region with $T_3 = 9.1$ keV, $abund_3 = 0.27$ Solar.

Comparison of this model ($\equiv$3T model, see Fig. 8) with the spectrum of the full 7 arcmin region shows that there are some problems. There appears an un-modeled emission feature at 1.2 keV which cannot be explained by background uncertainties (see Molendi & Gastaldello 2009, for a discussion of a similar feature in case of Perseus cluster). For the purpose of this work, we noted that excluding the $1.1-1.3$ keV band from our spectral fits did not produce a significant change to the results. Also, there are systematically increasing residuals in the energy range $0.6-1.0$ keV at the $\sim 5\%$ level. Furthermore, the Fe XXV and XXVI lines are not well modeled (see below). We note that the large number of photons ($\sim 10^6$) in the Ophiuchus spectrum renders the statistical uncertainties small ($\sim 2-10\%$ in the $0.6-7.4$ keV band) even with the original binning. It is possible that remaining calibration uncertainties of the total efficiency of PN at this level become important due to the high statistical precision of the data.
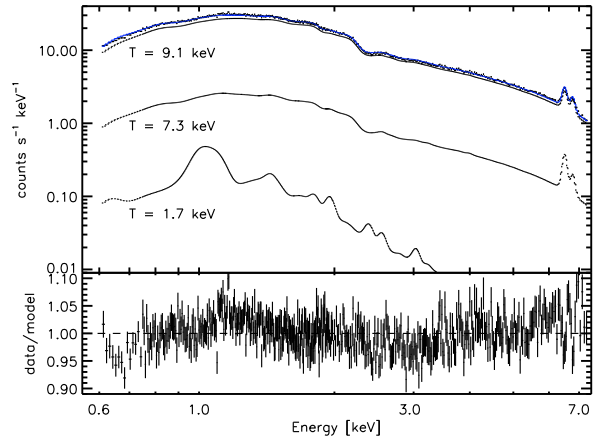

Fig. 8. In *the upper panel* the crosses show the PN data and statistical uncertainties from the central $r = 7$ arcmin region. The blue line shows the best-fit 3T model. The emission model components are also shown separately as solid lines. The *lower panel* shows that ratio of the data and the model prediction.

Note that we have assumed here that the non-thermal component does not affect the fits. Thus, when including the INTEGRAL data and a model for the non-thermal emission, we will examine and discuss the modifications to the thermal modelling.

6. Joint XMM-Newton and INTEGRAL analysis

With the thermal emission modeled, we then proceeded to a joint XMM-Newton – INTEGRAL modelling of the total emission in a very wide band, $0.6-140$ keV, of the central circular region within a radius of 7 arcmin.

6.1. PN/ISGRI cross-calibration

When comparing the different instruments, we noted that the central 7 arcmin area covered by PN is obscured by 8% due to CCD gaps and bad pixels.

Given that the Ophiuchus cluster shows an angular extent larger than the PSF of IBIS/ISGRI, for a correct cross-calibration between the different instruments it is necessary to know the fraction of the flux extracted by ISGRI compared to the total flux in a radius of 7 arcmin used for the PN spectral extraction
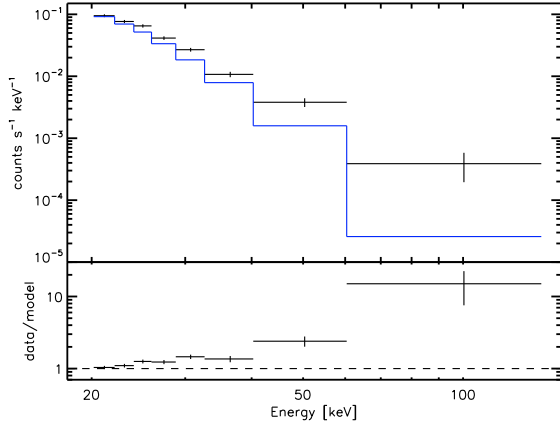
Fig. 9. In *the upper panel* the crosses show the ISGRI data, while the blue line shows the best-fit 3T model extrapolation from the PN analysis. The *lower panel* shows the ratio of data and model prediction.

(see below). To estimate this number, we computed the shadow pattern cast by the source using the surface-brightness profile as measured by XMM/MOS2 (see Eckert et al. 2007; and Renaud et al. 2006, for the details), and simulated raw ISGRI detector images with Poissonian background in each energy band. Then we extracted the spectra in the standard way and computed the total flux extracted by the software. As a result, we found that ISGRI extracts 84% of the total injected flux.

We assumed that the ∼6% difference in the covered area between PN and INTEGRAL does not significantly change the spectral shape and we thus multiplied the model normalisations with the covering fractions in the fitting models so that both obtained best-fit model normalisations correspond to a full unobscured $r = 7$ arcmin circular region. We additionally allowed 10% variation between the above PN–ISGRI normalisation factor due to systematic uncertainties in the PN/ISGRI cross-calibration.

6.2. Excess emission

The prediction of the 3T thermal model derived with XMM-Newton data in Sect. 5.3 fails to reproduce the ISGRI data at energies above 25 keV (see Fig. 9). Combining the effect of the statistical uncertainties of the thermal model parameters and the statistical uncertainties of the ISGRI data we found that the ISGRI data exceeds the model prediction by 5.7σ in the 20−140 keV band, by a maximum difference of a factor of ∼10 at 100 keV, similar to the results in Eckert et al. (2008).

To quantify the effect of the excess emission observed by ISGRI we fitted the ISGRI data in the 20−140 keV band using a single-temperature MEKAL model (abundance fixed to 0.3 Solar). The resulting temperature value is $T = 11.6 \pm 0.6$, i.e. much higher than the hot component measured with PN (9.1 ± 0.1 keV). The best-fit thermal model to 20−80 keV band of ISGRI data in the central 7 arcmin region (scaled to the full unobscured region based on simulations, see Sect. 6.1) yields a flux of ∼4.5×10^{-11} erg s^{-1} cm^{-2} in this band. Note that this model does not fit well the data at the highest energies. Since the detection of radio emission proved the existence of relativistic electrons in Ophiuchus (Govoni et al. 2009) we assume in the following that the excess emission found here is non-thermal.

Because of the broad PSF of IBIS/ISGRI (12 arcmin *FWHM*), we cannot exclude the possibility that the hard X-ray excess detected by INTEGRAL would be due to

a highly-obscured Seyfert nucleus, which would be hidden in the soft X-ray band (1−10) keV due to high *NH*. However, the population studies of AGN in hard X-rays by INTEGRAL (Beckmann et al. 06, Paltani et al. 08) and Swift (Tueller et al. 08) have shown that there is no evidence for such a Compton thick AGN population which is not detected in the soft X-rays. In order to examine this issue quantitatively, we used ISGRI data of Ophiuchus to examine the possible time variability produced by AGN in the field. We extracted spectra from periods March 28, 2003 – August 23, 2004; August 26, 2004 – September 22, 2005 and September 22, 2005 − September 14, 2007. The exposure times are 1.1, 0.8 and 1.2 Ms. The resulting spectra are consistent within the statistical uncertainties: The best-fit MEKAL spectra yield consistent temperatures (12.2 ± 1.0 keV, 12.3 ± 1.3 keV, 10.6 ± 0.9 keV) and 20−80 keV band fluxes[2] ($4.7 \pm 0.4 \times 10^{-11}$ erg s^{-1} cm^{-2}, $4.5 \pm 0.5 \times 10^{-11}$ erg s^{-1} cm^{-2} and $4.3 \pm 0.3 \times 10^{-11}$ erg s^{-1} cm^{-2}), respectively for the different periods. Thus, these data indicate no variability in the Ophiuchus hard spectrum during the 4 years of observations which argues against a significant AGN contribution.

6.3. Modelling the inverse compton scattering of CMB photons

The usual mechanism for explaining the hard X-ray excess in clusters is the inverse compton scattering (IC) of the cosmic microwave background (CMB) photons by the relativistic cluster electrons (e.g. Sarazin 1988). We examined this scenario by performing spectroscopy to PN and ISGRI data in the following. If the same population of relativistic electrons produces both the synchrotron emission and the IC, the spectral indices of the two power-law spectra should be equal. Unfortunately this test is not yet possible, because the radio halo in Ophiuchus has been significantly detected only at one wavelength. While keeping the thermal model fixed to the above 3T model, we added a simple power-law and its variants i.e. with two photon indices on both sides of a break energy (broken power-law) or with an exponential high energy cut-off (cutoff power-law) to the spectral model. When deriving the thermal model above we assumed that the non-thermal emission is negligible at energies below 10 keV, compared to the thermal emission. This requires a very hard simple power-law and such a model cannot reproduce the ISGRI data well. Using the broken power-law and cutoff power-law models the photon index becomes negative at energies below 10 keV. Since such models are unphysical, we then allowed in the following the hot component of the 3T model (the MEKAL model with $T \sim 9$ keV) to be modified by the addition of the non-thermal component. We kept the central cooler components fixed because the thermal emission is so bright in the centre that it probably dominates the emission.

The resulting best-fit model has a steep power-law, with $\alpha_{ph} = 3.4 \pm 0.2$. The *NH* obtains a very high value, $0.44 \pm 0.02 \times 10^{22}$ cm^{-2}, much higher than that derived from the IRAS and Copernicus data (see Sect. 5.1). Also, the model underpredicts the ISGRI data significantly at $E > 40$ keV. The high level of background emission results in large statistical uncertainties in the ISGRI data (∼50% at 100 keV), and thus the statistical weight of ISGRI data is negligible compared to that of PN. This is demonstrated by the fact that when excluding the ISGRI data from the fit the power-law properties are consistent with those

---

[2] The fluxes are scaled to the full $r = 7$ arcmin circular region based on the simulations in Sect. 6.1.
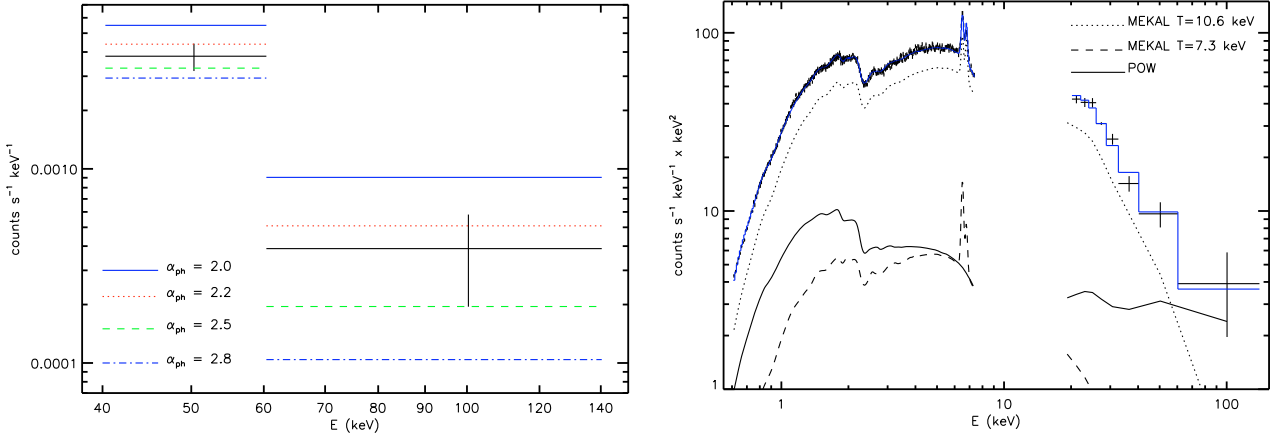
Fig. 10. The black crosses show the data and the statistical uncertainties. In the *left panel* only the ISGRI data above 40 keV energies are shown, together with the prediction of the 3T mekal + power-law model with different values for the photon index. In the *right panel* the PN and ISGRI spectra have been multiplied by E² for display purposes. The blue line shows the total best-fit convolved and absorbed model with $\alpha_{ph} \equiv 2.3$. The following components of the total model are also shown separately: power-law (solid line), hot thermal component (dotted line) and the thermal component due to the cooling in the centre (dashed line).

in the joint PN+ISGRI fit above. It is unfortunate that the statistical weight of the data is smallest, where the signal is relatively strongest: The emission of the thermal model decreases exponentially at energies above 10 keV, while the non-thermal component is assumed to have a power-law spectrum. Thus a larger fraction of the ISGRI data consists of non-thermal emission, compared to PN. The PN data dominate the fit and thus small uncertainties of the modelling of the thermal emission due to problems of e.g. *NH* or the PN calibration (see Sect. 5) may weigh more than the real ISGRI data.

We thus proceeded by fitting the data while fixing the photon index to a value in the range [1.5−3.0], allowing *NH* and the hot emission component parameters to vary. We visually examined how well each of the forced best-fit models matches the ISGRI data. We found that models with α_{ph} = 1.5 are too hard compared to the ISGRI data. With higher photon index the models fit the ISGRI data better, until they underpredict the data. The best agreement with the ISGRI data is obtained in the range 2.2−2.5 (see Fig. 10). These models fit the PN data significantly better than the 3T models fitted to PN data only (see Sect. 5.3): the overall residuals are smaller and the χ^2/d.o.f. decreases significantly from 800.95 to 690−693 for 1 additional free parameter and 500 data bins.

6.3.1. Results

We will use the above models in the following to present the results. The presented ranges of the parameters are not statistical 1σ uncertainties, but rather show the variation of the best-fit parameters in the models with α_{ph} fixed to range 2.2−2.5. Assuming that the IC and radio emission are produced by the same population of relativistic electrons (e.g. Sarazin & Lieu 1998) i.e.,

$$N(\gamma) = N_1 \times \gamma^{-p}, \quad (1)$$

the implied differential momentum spectra of the relativistic electrons has a slope *p* of 3.4−4.0. The corresponding range of the radio spectral index is 1.2−1.5. This is consistent with the estimated upper limit of 1.7 for the radio spectral index in Ophiuchus (Pérez-Torrez et al. 2009). The implied radio index ~1.5 is at the border of that predicted by the primary and

secondary models (e.g Ferrari et al. 2008) and thus we cannot distinguish those models with the current data.

In these models the flux of the power-law component in the 1−10 keV band is ~10% of the total. The 20−80 keV band flux is $0.5-1.5 \times 10^{-11}$ erg s⁻¹ cm⁻². The BeppoSAX PDS analysis of Ophiuchus (Nevalainen et al. 2004), while covering a much larger region, yielded a consistent 1σ upper limit of 1.6×10^{-11} erg s⁻¹ cm⁻² for the non-thermal flux in the 20−80 keV band for α_{ph} = 2.0 (Nevalainen et al. 2004). The 90% upper confidence limit obtained with BAT using α_{ph} = 2.0 (converted to the 20−80 keV band) is 0.9×10^{-11} erg s⁻¹ cm⁻² (Ajello et al. 2009). Our hardest model ($\alpha_{ph} \equiv 2.2$) exceeds this value significantly, while our other accepted models agree with the BAT value.

Using the formula for the power emitted by an electron through inverse compton scattering (e.g. Rybicki & Lightman 1979) and using the electron distribution of Eq. (1), one obtains a relation between the IC luminosity and relativistic electron distribution as

$$\frac{L_{IC}}{V} = \frac{4}{3} \sigma_T c u_\gamma N_1 \frac{\gamma_{max}^{3-p} - \gamma_{min}^{3-p}}{3-p}, \quad (2)$$

where L_{IC} is the luminosity of the IC component in energy range $[\gamma_{min}, \gamma_{max}]$, *V* is the emitting volume, σ_T is the Thompson cross section ($\approx 6.652 \times 10^{-25}$ cm²) and u_γ is the energy density of the CMB ($\approx 4.356 \times 10^{-13}$ erg cm⁻³). Our full energy band of 0.6−140 keV band corresponds to $\gamma_{min} \sim 800$ and $\gamma_{max} \sim 13\,000$. For Ophiuchus, the power-law component with a photon index of 2.3 yields a luminosity of $L_{IC} \sim 1.3 \times 10^{44}$ erg s⁻¹ in this band. Approximating the emitting volume as a sphere of 7 arcmin radius, we use volume $V = 1.5 \times 10^{72}$ cm³. Using *p* = 3.6, as given by α_{ph} = 2.3, Eq. (2) yields a normalisation $N_1 \sim 2.7$ cm⁻³ for Ophiuchus. Now the electron population (Eq. (1)) is fully solved and we can compute the pressure of the relativistic electron population (P_{IC}) using

$$P_{IC} = \frac{E}{3V} = \frac{1}{3} \int_{\gamma_{min}}^{\gamma_{max}} N(\gamma) \gamma m_e c^2 \, d\gamma$$

$$= \frac{m_e c^2 N_1}{3} \int_{\gamma_{min}}^{\gamma_{max}} \gamma^{1-p} \, d\gamma = \frac{m_e c^2 N_1}{3} \frac{\gamma_{max}^{2-p} - \gamma_{min}^{2-p}}{2-p} \quad (3)$$
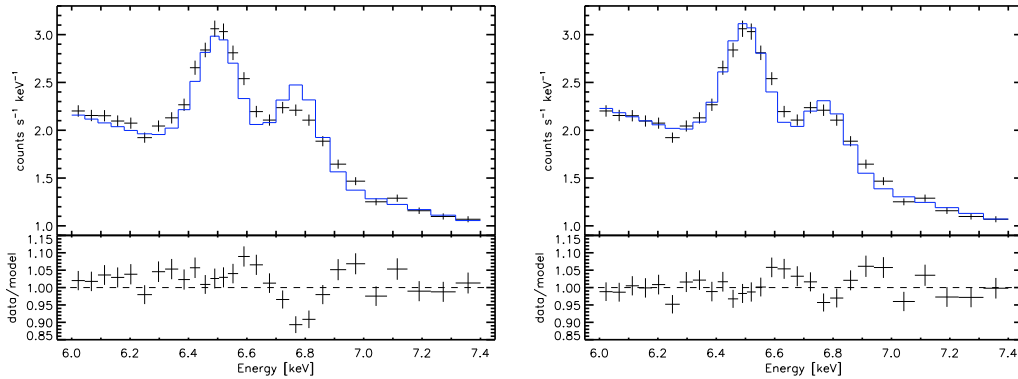
Fig. 11. The crosses in the *upper panels* show the PN spectrum of the central $r = 7$ arcmin region in the 6.0−7.4 keV band. The blue line shows the convolved best-fit model when fitting the 0.5−100 keV band with a 3T+pow model with $\alpha_{ph} \equiv 2.3$ (*left panel*) and when fitting the 6.0−7.4 keV band with a single-temperature model (*right panel*). The *lower panels* show the ratio of the data and the model prediction.

yielding a value 1.1×10^{-12} erg cm^{-3}. On the other hand, the pressure of the thermal electrons is given by $P_{ther} = n_{e,ther} kT_{gas}$. The values within $r = 7$ arcmin sphere in Ophiuchus ($n_{e,ther} \sim 6.4 \times 10^{-3}$ cm^{-3} and $T_{gas} \sim 9$ keV) yield $P_{ther} \sim 9.2 \times 10^{-11}$ erg cm^{-3}. Thus the pressure of the non-thermal electrons is $\sim 1\%$ of that of the thermal electrons. Thus there is no problem of confining the relativistic electron population in the gravitational potential of the cluster.

The VLA observations of Ophiuchus at 1.4 GHz yielded the flux of the mini-halo (see Fig. 4) as ~ 106 mJy within a radius 9.6 arcmin (Govoni et al. 2009; Murgia et al. 2009). Using the measured exponential profile for the radio surface brightness in the above work, we obtained a mini-halo brightness of 85 mJy within our extraction region of $r = 7$ arcmin. We used this value together with the properties of the above power-law models to calculate the magnetic field strength using the formulation of Sarazin (1988). The calculations yield $B = 0.05-0.15$ μG, consistent with those derived in several other clusters (e.g. Rephaeli et al. 2008).

Due to the lack of a major merger in mini-halo clusters, two possibilities remain for the acceleration mechanism of electrons (e.g. Ferrari et al. 2008): i) primary old merger and subsequent re-accelerations due to turbulence or ii) secondary hardonic collisions. In Ophiuchus, the secondary acceleration models due to hadron-hadron collisions are inconsistent with the available hard X-ray measurements (Colafrancesco & Marchegiani 2009). A viable scenario for the Ophiuchus cluster is that the primary merger happened sufficiently long time ago (as required by the long cooling time) so that most merger signatures have disappeared and that the relativistic electron population was later re-accelerated by the MHD turbulence. This is further supported by the steepness of the implied radio index (1.2−1.5) which suggests that the electron population has experienced significant ageing. The relatively low magnetic strength derived in this work is qualitatively consistent with the primary/turbulence model: in a strong shock the magnetic field is amplified, so we would expect higher B field values. With time, the magnetic field decays and the particles move away from the shock regions, so one would expect lower magnetic field values in case of an aged population.

7. Discussion

When we added the power-law component to the model (see Sect. 6.3.1), the resulting temperatures of the hot component

(10.5−10.9 keV) became much higher than those derived with the Fe XXV/XXVI ratio (~ 9 keV, see Sect. 5). We verified with simulations that the presence of the power-law component with the above parameters does not bias the temperature measured with the Fe lines. The Fe XXV line emission is underpredicted while the Fe XXVI line emission is overpredicted, both at 10−15% level, with the models presented here (see Fig. 11). We note that when we fitted only the 6.0−7.4 keV band with a single-temperature model, some residuals still remained at a 5% level (see Fig. 11). This indicates some uncertainties in the modelling of the energy redistribution or reconstruction of the photon energy (addressed elsewhere), or that the Fe line ratio deviates from the thermal prediction.

We experimented with the XSPEC model gsmooth, as Molendi & Gastaldello (2009) in case of Perseus, to see whether the suggested mis-calibration of PN energy resolution is affecting the fits. Using the proposed values (4 eV at 6 keV for the Gaussian width and -1 for the power-law index) we obtained a very small change in the residuals, and in the direction of increasing the χ^2. Allowing the Gaussian width to vary does not improve the fit. Thus, the possible miscalibration of the energy resolution does not produce the residuals. This indicates at least two possibilities: either the real Fe XXV/XXVI line ratio is bigger than the thermal prediction, or the assumed IC/CMB scenario or its modelling is wrong.

Our adopted method of simple addition of a power-law component to the emission model ignores the possible effect of the non-thermal electrons to the ionisation balance. For instance, Prokhorov et al. (2009) showed that a presence of a population of supra-thermal electrons would decrease the Fe XXV/XXVI flux ratio compared to that in the case of pure Maxwellian velocity distribution of electrons (as assumed in our work). This model may also produce a continuum that is different from the power-law. Note that this mechanism does not produce the (observed) synchrotron emission and thus we still need the IC/CMB mechanism at a lower level. A detailed analysis of this possibility (i.e. the co-existence of thermal, supra-thermal and relativistic electrons in the cluster volume) will be carried out in another paper.

Alternately, assuming that the Fe XXV/XXVI line ratio is correctly reproduced by the MEKAL model, we need to modify the modelling of the non-thermal component. The power-law shape itself should be the correct model in the IC/CMB case, since the assumed diffusive shock acceleration process (Bell 1978) does produce relativistic electron populations with a power-law distribution. Also the radio spectra in cluster haloes

do have power-law shape (e.g. Ferrari et al. 2008). Thus, we need to search for different physical mechanisms than IC/CMB that would produce the non-thermal emission spectrum different from a power-law.

8. Conclusions

We analysed the central $r = 7$ arcmin region of the Ophiuchus cluster of galaxies using data obtained with the XMM-Newton EPIC and INTEGRAL ISGRI instruments. The ISGRI data yielded a 5.7σ detection of excess emission in the $20-120$ keV band over the thermal prediction, as modeled with PN data. Our XMM-Newton analysis confirmed the existence of a cool core in Ophiuchus. The derived very long cooling time (3×10^9 yr) as well as the lack of significant merger signatures argues against a recent major merger in the Ophiuchus centre. These features are consistent with most clusters hosting a radio mini-halo (Ferrari et al. 2008), which has also been detected in Ophiuchus (Govoni et al. 2009).

In most proposed models for the non-thermal emission in clusters the same population of relativistic electrons produces both the radio emission (via synchrotron) and hard X-ray emission (via inverse compton scattering of the cosmic microwave background photons). Our results support this scenario, since the derived photon index of $2.2-2.5$ for the non-thermal component corresponds to radio index of $1.2-1.5$ with is consistent with the upper limit (1.7) derived from the radio observations of Ophiuchus (Péres-Torrez et al. 2009).

The non-thermal component produces $\sim$10% of the total flux in the $1-10$ keV band. These models imply a differential momentum spectrum of the relativistic electrons with a slope of $3.4-4.0$ and a magnetic field strength $B = 0.05-0.15$ μG. The pressure of the non-thermal electrons is $\sim$1% of that of the thermal electrons, i.e. the gravitational potential of the cluster is adequate for confining such a population of non-thermal electrons.

References

Ajello, M., Rebusco, P., Cappelluti, N., et al. 2009, ApJ, 690, 367
Anders, E., & Ebihara, M. 1982, Geochim. Cosmochim. Acta, 46, 2363
Anders, E., & Grevesse, N. 1989, Geochim. Cosmochim. Acta, 53, 197
Ascasibar, Y., & Markevitch, M. 2006, ApJ, 650, 102
Baldi, A., Ettori, S., Mazzotta, P., et al. 2007, ApJ, 666, 835
Beckmann, V., Soldi, S., Shrader, C., et al. 2006, ApJ, 652, 126
Bell, A. 1978, MNRAS, 182, 147
Bohlin, R., Savage, B., & Drake, J. 1978, ApJ, 224, 132
Brunetti, G., Setti, G., Feretti, L., et al. 2001, MNRAS, 320, 365
Brunetti, G., Blasi, P., Cassano, R., et al. 2004, MNRAS, 350, 1174
Cavaliere, A., & Fusco-Femiano, R. 1976, A&A, 49 137
Colafrancesco, S., & Marchegiani, P. 2009, A&A, 502, 711
Courvoisier, T. J.-L., Walter, R., Beckmann, V., et al. 2003, A&A, 411, L53
De Luca, A., & Molendi, S. 2004, A&A, 419, 837
Dennison, B. 1980, ApJ, 239, L93
Eckert, D., Neronov, A., Courvoisier, T., et al. 2007, A&A, 470, 835
Eckert, D., Produit, N., Paltani, S., et al. 2008, A&A, 479, 27
Ferrari, C., Govoni, F., Schindler, S., et al. 2008, SSRv, 134, 93
Fujita, Y., Hayashida, K., Nagai, M., et al. 2008, PASJ, 60, 1133
Govoni, F., Murgia, M., Markevitch, M., et al. 2009, A&A, 499, 371
Hasegawa, T., Wakamatsu, K., Malkan, M., et al. 2000, MNRAS, 316, 326
Jourdain, E., Gotz, D., Westergaard, N., et al. 2008, in publication in the 7th INTEGRAL workshop - An INTEGRAL View of Compact Objects Proceedings [arXiv:0810.0646v1]
Kalberla, P., Burton, W., Hartmann, D., et al. 2005, A&A, 440, 775
Lebrun, F., Leray, J. P., Lavocat, P., et al. 2003, A&A, 411, L141
Markevitch, M., & Vikhlinin, A. 2007, PhR, 443, 1
Matsushita, K. 2001, ApJ, 547, 693
Molendi, S., & Gastaldello, F. 2009, A&A, 439, 13
Morrison, R., & McCammon, D. 1983, ApJ, 270, 119
Murgia, M., Govoni, F., Markevitch, M., et al. 2009, A&A, 499, 679
Nevalainen, J., Oosterbroek, T., Bonamente, M., et al. 2004, ApJ, 608, 166
Nevalainen, J., Markevitch, M., & Lumb, D. 2005, ApJ, 629, 172
Paltani, S., Walter, R., McHardy, I., et al. 2008, A&A, 485, 707
Perez-Torres, M., Zandanel, F., Guerrero, M., et al. 2009, MNRAS, 396, 2237
Pfrommer, C., & Ensslin, T. 2004, A&A, 413, 17
Poole, G., Fardal, M., Babul, A., et al. 2006, MNRAS, 373, 881
Prokhorov, D., Durret, F., Dogiel, V., et al. 2009, A&A, 496, 25
Renaud, M., Gros, A., Lebrun, F., et al. 2006, A&A, 456, 389
Rephaeli, Y., Nevalainen, J., Ohashi, T., et al. 2008, SSRv, 134, 71
Rybicki, G., & Lightman, A. 1979, Radiative processes in astrophysics (Wiley-Interscience publication)
Sarazin, G. 1988, X-ray emissions from clusters of galaxies (Cambridge Astrophys. Ser.)
Sarazin, G., & Lieu, R. 1998, ApJ, 494, L177
Schlegel, D., Finkbeiner, D., & Davis, M. 1998, ApJ, 500, 525
Tueller, J., Mushotzky, R., Barthelmy, S., et al. 2008, ApJ, 681, 113
Vikhlinin, A., Kravtsov, A., Forman, W., et al. 2006, ApJ, 640, 691
Winkler, C., Courvoisier, T. J.-L., Di Cocco, G., et al. 2003, A&A, 411, L1